Magma ascent mechanisms in the transition regime from solitary porosity waves to diapirism

Janik Dohmen[1], Harro Schmeling[1]

[1]Institute for Geoscience, Goethe University, Frankfurt, Germany

5   *Correspondence to:* dohmen@geophysik.uni-frankfurt.de

Abstract

In partially molten regions inside the earth melt buoyancy may trigger upwelling of both solid and fluid phases, i.e. diapirism. If the melt is allowed to move separately with respect to the matrix, melt perturbations may evolve into solitary porosity waves. While diapirs may form on a wide range of scales, porosity waves are restricted to

10   sizes of a few times the compaction length. Thus, the size of a partially molten perturbation controls whether a diapir or a porosity wave will emerge. We study the transition from diapiric rise to solitary porosity waves by solving the two-phase flow equations of conservation of mass and momentum in 2D with porosity dependent matrix viscosity. We systematically vary the initial size of a porosity perturbation from 1 to 100 times the compaction length. If the perturbation is much larger than a regular solitary wave, its Stokes velocity is large and

15   therefore faster than the segregating melt. Consequently, the fluid is not able to form a porosity wave and a diapir emerges. For small perturbations solitary waves emerge, either with a positive or negative vertical matrix velocity inside. In between the diapir and solitary wave regimes we observe a third regime of solitary wave induced focusing of melt. In these cases, diapirism is dominant but the fluid is still fast enough to locally build up small solitary waves which rise slightly faster than the diapir and form finger like structures at the front of the diapir. In

20   our numerical simulations the width of these fingers is controlled by the compaction length or the grid size, whichever is larger. In cases where the compaction length becomes similar to or smaller than the grid size the finger-like leading solitary porosity waves are no more properly resolved, and too big and too fast waves may be the result. Therefore, one should be careful in large scale two-phase flow modelling with melt focusing especially when compaction length and grid size are of similar order.

25   **1 Introduction**

In many scenarios inside the earth the process of a fluid moving relatively to a viscously deformable porous matrix is an important transport mechanism. The physics of these scenarios were firstly described by McKenzie (1984) and it was later shown by several authors that these equations allow for the emergence of solitary porosity waves (Scott & Stevenson, 1984; Barcilon & Lovera 1989; Wiggins & Spiegelman, 1995). Porosity waves are regions of

30   localized excess fluid that ascend with permanent shape and constant velocity, controlled by compaction and decompaction of the surrounding matrix.

Even though these porosity waves were of vast interest for many authors over the last decades and the possible consequences on geochemistry and fluid flow in lower and middle crust in general (e.g. Watson & Spiegelman, 1994; McKenzie, 1984; Connolly, 1997; Connolly & Podladchikov, 2013, Jordan et al., 2018, Richard et al., 2012)

35   or the effects of matrix rheology on porosity waves (e.g. Connolly & Podladchikov, 1998; Yarushina et al., 2015;

Connolly & Podladchikov, 2015; Omlin et al., 2017; Dohmen et al., 2019) have been examined, there are still open questions. One open question is that of the scaling. The size of a solitary porosity wave is usually of the order of a few compaction lengths (McKenzie, 1984; Scott & Stevenson, 1984; Simpson & Spiegelman, 2011), but this length scale varies over a few orders of magnitude, depending on the shear and bulk viscosity of the matrix, fluid

40   viscosity and permeability (see 1) with typical values of 100-10000 meters (McKenzie, 1984; Spiegelman, 1993).

On the other hand, partially molten regions in the lower crust or upper mantle are prone to gravitational instabilities such as Rayleigh-Taylor instabilities or diapirism (e.g. Griffith, 1986; Bittner and Schmeling, 1995; Schmeling et al., 2019). As characteristic wavelengths of Rayleigh-Taylor instabilities may be similar, but also of significantly different order of those of porosity waves, the question arises how these two mechanisms interact and how does

45   the transition between magmatic rise due to diapirism or porosity wave look like.

The extent of partially molten scenarios inside the earth's mantle vary over many orders of magnitude and this transition might have an important effect on the evolution of these regions. In this work we want to address this problem and look especially on what happens for different sizes of initial perturbations and what are the numerical implications on modelling magma transport.

50   ## 2 Theoretical Approach

2.1 Governing equations

The equations shown here describe the relative movement between matrix and fluid and are based on the equations of McKenzie (1984), Schmeling (2000), and Schmeling et al. (2019). The mathematical description is applied to solitary waves, which was already described in detail in Dohmen et al. (2019) and will only be briefly shown.

55   The following equations are non-dimensionalized using the compaction length in respect to the background porosity, which is given by

$$\delta_{c0} = \left(\frac{\eta_{b0} + \frac{4}{3}\eta_{s0}}{\eta_f} k_{\varphi 0} \right)^{\frac{1}{2}},$$ (1)

and the scaling separation velocity, based on the Darcy velocity, given by

$$v_{sc0} = \frac{k_{\varphi 0}}{\eta_f \varphi_0} (\rho_s - \rho_f) g.$$ (2)

60   The subscript 0 refers to the background porosity φ_0 which is used to calculate the permeability, given by

$$k_\varphi = k_0 \varphi^n,$$ (3)

and the shear and bulk viscosity:

$$\eta_s = \eta_{s0}(1 - \varphi),$$ (4)

$$\eta_b = \eta_{s0} \frac{1 - \varphi}{\varphi}.$$

Here η_{s0} is the intrinsic shear viscosity, η_f the viscosity of the fluid, ρ_s and ρ_f the density of the solid and fluid

65   assumed to be constant, respectively, and g the gravitational acceleration. n is the permeability-porosity dependency exponent and for all models taken to be 3. In contrast to Dohmen et al. (2019) we here use these simplified equations for the viscosity as they are commonly used. The influence of more realistic, lower viscosities is only important for higher melt fractions than those that are used here (Dohmen et al., 2019).

All quantities can be non-dimensionalized using

$$\vec{x} = \delta_{c0}\,\vec{x}' \qquad \vec{v} = v_{sc0}\vec{v}' \qquad t = \frac{\delta_{c0}}{v_{sc0}}t' \qquad \tau_{ij} = \eta_{s0}\frac{v_{sc0}}{\delta_{c0}}\tau_{ij}' \qquad (5)$$

$$\eta = \eta_{s0}\eta' \qquad \rho = \rho_s\rho' \qquad \varphi = \varphi_0\varphi'.$$

70   where the primed quantities are non-dimensional. The resulting equations for mass of solid and fluid, respectively, are

$$\frac{\partial(1 - \varphi_0\varphi')}{\partial t'} + \vec{\nabla}' \cdot \left((1 - \varphi_0\varphi')\vec{v}_s'\right) = 0 \qquad (6)$$

and

$$\frac{\partial \varphi'}{\partial t'} + \vec{\nabla}' \cdot \left(\varphi'\vec{v}_f'\right) = 0. \qquad (7)$$

In the limit of small fluid viscosity, the momentum equation of the solid-fluid mixture is

$$\left(\frac{\partial^2}{\partial x'^2} - \frac{\partial^2}{\partial z'^2}\right)\left[\eta_s'\left(\frac{\partial^2\psi'}{\partial x'^2} - \frac{\partial^2\psi'}{\partial z'^2}\right)\right] + 4\frac{\partial^2}{\partial x'\partial z'}\left[\eta_s'\frac{\partial^2\psi'}{\partial x'\partial z'}\right] = \varphi_0^2\frac{\eta_{b0} + \frac{4}{3}\eta_{s0}}{\eta_{s0}}\frac{\partial\varphi'}{\partial x'} + A(\chi') \qquad (8)$$

with

$$A(\chi') = -2\frac{\partial^2}{\partial x'\partial z'}\left[\eta_s'\left(\frac{\partial^2\chi'}{\partial x'^2} - \frac{\partial^2\chi'}{\partial z'^2}\right)\right] + 2\left(\frac{\partial^2}{\partial x'^2} - \frac{\partial^2}{\partial z'^2}\right)\left[\eta_s'\frac{\partial^2\chi'}{\partial x'\partial z'}\right]. \qquad (9)$$

75   Here ψ describes the incompressible flow and χ the irrotational, compaction flow velocity, so that the solid velocity can be written as (following Šrámek *et al.*, 2007)

$$\vec{v}_s = \vec{v}_1 + \vec{v}_2 = \begin{pmatrix} \frac{\partial\psi}{\partial z} \\ -\frac{\partial\psi}{\partial x} \end{pmatrix} + \begin{pmatrix} \frac{\partial\chi}{\partial x} \\ \frac{\partial\chi}{\partial z} \end{pmatrix}. \qquad (10)$$

For the momentum equation of the fluid we have

$$\vec{v}_f' - \vec{v}_s' = \varphi'^{n-1}\left((1 - \varphi_0\varphi')\vec{e}_z - \frac{\eta_{s0}}{\left(\eta_{b0} + \frac{4}{3}\eta_{s0}\right)}\frac{1}{\varphi_0}\frac{\partial\tau_{ij}'}{\partial x_j'}\right). \qquad (11)$$

τ_{ij} is the effective viscous stress tensor of the matrix

$$\tau_{ij} = \eta_s \left(\frac{\partial v_{si}}{\partial x_j} + \frac{\partial v_{sj}}{\partial x_i} \right) + \left(\eta_b - \frac{2}{3}\eta_s \right) \delta_{ij} \vec{\nabla} \cdot \vec{v}_s. \tag{12}$$

$\vec{e}_z$ is the unit vector in opposite direction to gravity. For a more detailed description of the theory see Dohmen et
80   al. (2019).

2.2 Model setup

The model consists of a $L' x L'$ box with a background porosity, φ_0, of 0.5%. L' is the the non-dimensional side
length of the box. A non-dimensional Gaussian wave porosity anomaly is placed at $x_0' = 0.5\,L'$ and $z_0' = 0.2\,L'$.
It has the form of

$$\varphi = \varphi_0 A \cdot \exp\left(-\left(\frac{x' - x_0'}{w'} \right)^2 - \left(\frac{z' - z_0'}{w'} \right)^2 \right) \tag{13}$$

85   where A is the non-dimensional amplitude and w' the non-dimensional half-width of the wave. w' in the model is
always equal to $0.05L'$. To vary the radius of the anomaly in terms of compaction lengths we change the
characteristic compaction length of the whole model, which is equivalent to changing L' accordingly. While the
radius of an emerging solitary wave is always in the order of a few compaction lengths, by varying L', the radius
of the initial anomaly is varied between 1 and 100 times the compaction length to explore the parameter range in
90   which diapirs might become dominant. The model box has always the same resolution, but the compaction length
is differently resolved for each model.

At the top and the bottom, we prescribe an out- and inflow for both melt and solid, respectively, which is calculated
analytically for the background porosity. At the sides we use mirroring boundary conditions.

2.3 Calculation of the Stokes velocity

95   Assuming that an initial porosity anomaly may diapirically rise due to buoyancy we want to compare this kind of
Stokes velocity with the phase velocity of a resulting solitary wave. The Stokes velocity applied to the partially
molten Gaussian wave in a background porosity can be written as

$$v_{st} = C\frac{(\rho_s - \rho_f)\varphi_{max}r^2 g}{\eta_s}, \tag{14}$$

where $\varphi_{max} = \varphi_0 \cdot A$ and C is a geometric constant. In the classical Stokes formula r is the radius of the Stokes-
sphere. Here we choose r as the half width of the porosity anomaly.

100   Using the compaction length and the scaling separation velocity this equation can be non-dimensionalized to

$$v_{st}' = C\frac{\left(\eta_b + \frac{4}{3}\eta_s\right)\varphi_0^2 A r'^2}{\eta_s}. \tag{15}$$

r' is now the half width of the wave in terms of compaction length. As this radius and the maximum melt fraction
change strongly during the run of a model we calculate this radius for every timestep by searching for the maximum
melt fraction in the model and then look for the horizontal half width of the porosity anomaly. The vertical half
width cannot be used as the wave drags a veil with it while ascending, but still the received values give decent
105   radii. Using the Stokes-formula of a (2D) horizontal cylinder rising in a horizontal (2D) fluid cylinder of larger

radius, we find for a ratio of radii similar to the ratio of the half width of the porosity wave to the box size that C is of the order of a spherical Stokes sphere, i.e. C = 0.5.

3 Results

3.1 The transition from porosity wave to diapirism: Varying the initial wave radius

110   In this model series we vary the initial wave radius to cover the transition from porosity waves to diapirs. For small radii ($r' \leq 10$) we can clearly see the emergence of solitary waves (Fig. 1 top row). $r' = 1.5$ leads to a wave that is nearly the size of the initial perturbation. Even smaller radii would lead to bigger waves but with a smaller porosity amplitude as the melt needs to be conserved. For bigger radii the resulting solitary waves become smaller and lead to a focusing of melt. With an initial radius of 10 the resulting wave has just a size of ~20% the initial

115   wave size after it has risen half a box length.

For greater radii it is not clear if one can observe solitary waves. We still see a focusing of melt in a small peak of just a grid length in size (e.g. $r' = 20$). This small focusing might be a solitary wave that might be even smaller but is not able to focus more because the resolution does not allow for it. For the following radii ($r' > 20$) the elongation due to the focusing becomes smaller and smaller until it completely disappears at $r' > 40$. Here we

120   observe clear diapirism.

For the models in the transition zone ($8 \geq r' \geq 40$) it seems like the phase velocity of the evolving solitary wave becomes smaller compared to the remaining magmas rising velocity, that couldn't be focused. For $r' = 40$ we can still observe a small focusing that is just at the very top of the rising magma perturbation and has nearly the same velocity as the actual porosity perturbation. Due to that fact the shape of this rising magma anomaly is different to the diapirs and solitary waves and has a more finger like shape with accumulated melt at the top. In the diapir

125   regime all perturbations evolve similar with a comparable velocity and in the same shape.

3.2 Comparison with Stokes velocity

The velocity of a Stokes sphere for a certain radius increases linearly with amplitude and can be compared with a solitary waves' dispersion curve (Fig. 2). The dashed curves give the dispersion curves of 2D solitary waves with

130   different n-values in the permeability relation, while m= 0 or 1 correspond to cases with bulk viscosity equal to shear viscosity and variable bulk viscosity (as given by equation 4), respectively (Simpson and Spiegelmann, 2011). The porosity wave modelled in the previous section would correspond to n=3, m=1. On first sight the comparison of Stokes and porosity wave velocities correlates nicely with the transition from diapirism to solitary waves shown in Fig. 1: For bigger radii the Stokes velocities are higher than the solitary wave velocity and the

135   latter is therefore not the driving force of the ascending process and consequently not able to build up. For small radii the solitary wave velocity is clearly higher and therefore able to build up. Just by comparison of these curves, perturbations with $r' > 20$ should lead to diapirism while $r' < 20$ should lead to solitary waves.

As the solitary wave is still an attractor it leads to focusing in models where Stokes and solitary wave velocity are in the same order and leads to strongly different evolutions of the initial perturbation. We therefore calculate the

140   radius of the leading perturbation for every time step and use it to get its Stokes velocity. For $r' = 40$ (Fig. 3a) the Stokes velocity, calculated with the initial radius (red line), would be faster than the solitary wave (dashed line), but with the updated radius, in the porosity field plot (Fig. 3a top) we see that shortly after the start of the model

the solitary wave attracts some melt und builds up a tip of melt with a very small radius. This reduces the local Stokes velocity with time (orange curve) towards values below the dispersion curve. Thus, within the melt rich

145   tip, melt rises locally predominantly by two-phase flow. We therefore observe a large diapirically rising perturbation with a melt peak or tip at its front partly rising as a small solitary wave. The temporal evolution of the total rising velocity and amplitude of the melt anomaly is shown by the blue curve, starting from high velocity and amplitude values. Interestingly, the interaction of diapiric and two-phase flow rise leads to total velocities somewhat higher than the sum of the pure initial Stokes velocity (red curve) and pure solitary wave (dashed curve).

150   For $r' = 50$ the Stokes velocity of the leading perturbation (orange curve) also decreases shortly after start of the model but ends up in the same order as the dispersion curve. For this case we observe a rising perturbation which looks different to the normal diapirs. The attracting solitary wave rises inside the perturbation, it is not able to catch up and to form an even narrower solitary wave tip as in the r'=40 case, but still attracts some melt at the upper part of the perturbation. Consequently, a different distribution of accumulated melt in the upper part forms

155   without a tip. For $r' = 100$ the Stokes velocity is always faster, and the solitary wave is not able to attract melt which is too slow. This leads to clear diapirism, no two-phase flow melt accumulation within the upper part of the anomaly occurs anymore. The increase of the updated Stokes velocity with decreasing amplitude is due to the boundary effects at the top. As the plume approaches the top, the plume head widens, and the calculated radius is no longer appropriate to represent the shape of the perturbation.

160   It is interesting to note that (a) for the diapiric case (= 100 or larger, Fig. 3c) the total velocity (blue curve) approaches the Stokes velocity, that (b) for transition zone cases ($r' \leq 40$) the rising velocity approaches the dispersion relation of solitary waves (not shown), but (c) for transitional cases (e.g. $r' = 50$) the rising velocity of the wave is significantly higher (blue curve) than just the sum of the Stokes (red curve) and dispersion velocity of the solitary wave (dashed line in Fig. 3). We conjecture that within a rising Stokes sphere of radius larger than a

165   solitary wave the internal circulation promotes the rise of a porosity wave and the local Stokes sphere stress field may deform a circular porosity wave into a finger like geometry. Limited numerical resolution inhibits further focusing on these effects.

3.3 Effects on the mass flux

It is important to study the partitioning between rising melt and solid mass fluxes in partially molten magmatic

170   systems, because melts and solids are carriers of different chemical components. Within our Boussinesq approximation we may neglect the density differences between solid and melt. Then our models allow to evaluate vertical mass fluxes of solid or fluid by depicting the vertical velocity components multiplied with the melt or solid fractions, respectively:

$$q'_{sz} = (1 - \varphi_0 \varphi') \cdot v'_{sz}$$
$$q'_{fz} = \varphi_0 \varphi' \cdot v'_{fz}.$$

(16)

Figure 4 shows horizontal profiles through rising melt bodies at the vertical positions of maximum melt fraction.

175   The mass fluxes of solid and fluid are strongly affected by the change of the initial radius from the solitary wave regime to the diapiric regime. For $r' = 1.5$, where we observe a solitary wave, the fluid has its peak mass flux in the middle of the wave and the solid is going downwards, against the phase velocity. In the center the fluid flux is more than 10 times higher than the solid. The net upward flow in the center is balanced by the matrix dominated

downward flow outside the wave. For $r' = 10$ the wave area is much smaller and the ratio between solid and fluid

180 flux is around the order of one. Even though we observe a local minimum in the center of the wave for the solid flux it is not negative. However, the solid matrix around the wave is affected in a much greater area and, contrary to the case for $r' = 1.5$, the rising net mass flux in and around the melt anomaly is dominated by the solid rather than melt flux.

For $r' = 50$ and $r' = 100$ the solid flux is significantly higher than the fluid flux also within the melt anomaly.

185 So far, we have based our discussion of the transition between solitary waves and diapirs on qualitative model observations. We now try to invoke a more quantitative criterion. In a horizontal line passing through the anomalies porosity maximum we define the total vertical mass flux of the rising magma body by $\int_{\varphi'>1}(q_f + q_s)dx$ where the integration is carried out only in the region of increased porosity $\varphi > \varphi_0$, i.e. $\varphi' > 1$. This mass flux is partitioned between the fluid mass flux, $\int_{\varphi'>1} q_f dx$, and the solid mass flux, $\int_{\varphi'>1} q_s dx$. With these we define the

190 partition coefficients

$$C_{soli} = \frac{\int_{\varphi'>1} q_f dx}{\int_{\varphi'>1}(q_f + q_s)dx} \tag{17}$$

and

$$C_{dia} = \frac{\int_{\varphi'>1} q_s dx}{\int_{\varphi'>1}(q_f + q_s)dx} \tag{18}$$

The sum $C_{soli} + C_{dia}$ is always 1 and if $C_{soli} > C_{dia}$ then the solitary wave proportion is dominant, while for $C_{soli} < C_{dia}$ diapirism is dominant. In figure 5a these partition coefficients for several initial radii are shown. In red are the partition coefficients calculated at a horizontal line at the height of maximum melt fraction. The blue

195 dots are calculated for horizontal lines at all grid points below the maximum melt fraction as long as $\varphi' \geq \frac{\varphi_{max}}{2}$. For $r' = 1.5$, C_{soli} is equal to 1.5 and C_{dia} is equal to -0.5, i.e. we have a downward solid flux. With increasing radius C_{dia} increases until it changes its direction at $r' = 4$. For even bigger radii C_{dia} increases further until it approaches 1 at approximately $r' = 40$. C_{soli} changes so that the sum of both is always equal to 1. Even though diapirism is dominant for $r' > 7.5$ we observe solitary wave induced focusing until $r' = 40$ where the melt

200 segregation velocity $\overrightarrow{v_f}$ becomes slower than the matrix velocity $\overrightarrow{v_s}$. In figure 5b the ratio of maximum fluid velocity (i.e. $\overrightarrow{v_f}$) to absolute matrix velocity is shown. For small radii, where $C_{soli} \gg C_{dia}$, this ratio is approximately constant. The absolute velocity maxima itself are not constant but decrease with the same rate until the switch of negative to positive matrix mass flux, where the absolute matrix velocity starts to increase, while the fluid velocity keeps decreasing. At this zero crossing we would expect a ratio of infinity, but with our models we

205 are far enough away to not see it in the data. At $r' = 40$ the ratio decreased to 2 (i.e. $\overrightarrow{v_f} = \overrightarrow{v_s}$). From this point on the fluid is no longer able to focus into a solitary wave as the matrix is too fast and clear diapirism can be observed. The calculated partition coefficients at lower elevations show that within the point of maximum melt fraction, C_{soli} is highest and decreases behind the ascending peak. Apparently, the fluid is locally able to build up a solitary wave even though diapirism is dominant in the whole region. For small radii the partition coefficients vary strongest

210 because the melt fraction decreases strongly behind the center of the wave.

Based on these observations the evolution of these models can be divided into 3 regimes: (1) In the solitary wave regime ($r' \leq 7.5$) C_{soli} is larger than C_{dia} and the initial perturbation emerges into waves that have the properties of solitary waves and ascend with constant velocity and staying in shape. This regime can be further divided into 1a ($r' < 4$) ,where the solid mass flux is negative, and 1b ($4 < r' \leq 7.5$), where the solid moves upwards with

215   the melt. Waves in these regimes are very similar and differ only in the matrix flux.

In Regime (2) ($7.5 > r' \geq 40$) C_{dia} is bigger than C_{soli} but solitary wave induced focusing can be observed. Even though diapiric ascend is dominant, melt is locally able to focus into solitary waves because the fluid is still faster than the matrix. This leads to a small peak of high porosity, ascending as solitary wave, followed by a broader area ascending as diapir.

220   In regime (3) ($r' > 40$) the segregation velocity is smaller than the matrix velocity (i.e. $\frac{\max(v_f)}{\max(v_s)} \leq 2$) and the fluid is therefore no longer able to separate fast enough to build up a solitary wave. Dominated by solid mass flux a well-developed diapir will ascend.

4 Discussion

While in our models the compaction length was systematically varied but kept constant within in each model, our
225   results might also be applicable to natural cases in which the compaction length varies vertically. In the case of compaction length decreasing with ascent a porosity anomaly might start rising as a solitary wave but then passes through the transition towards diapiric rise. In this case the solitary wave would most certainly enter the regime 2 characterized by strong focusing followed by a bigger perturbation. A decreasing compaction length could be accomplished by decreasing the matrix viscosity or the permeability, or by increasing the fluid viscosity.
230   Decreasing matrix viscosity might be for example explainable by local heterogeneities, temperature anomalies for example due to secondary convective overturns in the asthenosphere or by a vertical gradient of water content, which may be the result of melt segregation aided volatile enrichment at shallow depths in magmatic systems. This could lead to the propagation of magma-filled cracks (Rubin, 1995) as already pointed out in Connolly & Podladchikov (1998). The latter authors have looked at the effects of rheology on compaction-driven fluid flow
235   and came to similar results for an upward weakening scenario. But this effect might not be strong enough to lead to the focusing needed for the nucleation of dykes. The decrease of permeability due to decrease in background porosity might be an alternative explanation. If a porosity wave reaches the top of a magma chamber the background porosity might decrease which would lead to focusing and eventually, when reaching melt free rocks, the melt rich fingers may stall as in our models at r' > 50 and the rising melt will accumulate and enter the pure
240   diapirism regime. But if the focusing is strong enough and the fluid pressure high enough this scenario could alternatively be a good explanation for the nucleation of dykes. Indeed, if the initiation of dyking is induced by melt channeling instabilities (Stevenson, 1989), our models constrain the minimum size for focused melt anomalies, namely a few compaction lengths. For a partially molten region subject to horizontal extensive stresses Stevenson (1989) determined the growth rate of a channeling instability and found that it reaches a flat maximum
245   plateau for wavelengths smaller than the order of the compaction length. Thus, at the top of our focused melt fingers the conditions for melt channeling and subsequent dyking may well be met.   Due to limited resolution in our models we are not able to test this combination of fingering and subsequent channeling on the sub-compaction length scale.

A big problem in this kind of modeling is of the numerical resolution. While one needs at least a few grid points
per compaction length to resolve a solitary wave decently, in some of our models this length scale drops to even
less than one grid point. In some cases, this should lead to solitary waves that are smaller than a grid length and
therefore the appearance of solitary waves is limited by the numerical resolution. Assuming that a typical radius
of a solitary wave is around five times the compaction length (Simpson & Spiegelman, 2011), for our model with
a resolution of 201x201, in all models with $r' \geq 50$ any typivcal solitary wave is not resolved by at least one grid
point (c.f. non-dimensional model sizes in Fig. 1 which are given in units of compaction lengths) . We already
observe an increase of supposed solitary wave diameter at around $r' = 30$ because the correct diameter cannot be
resolved anymore. Before that the diameters stay more or less constant, but even for smaller radii we observe
strong differences in evolution with resolution. For the $r' = 10$ case a test with a doubled resolution has shown
that the higher resolved model builds up a well-developed solitary wave while the lower resolved model shows
just a focusing into one grid point. The peak porosity in the lower resolved model ascends approximately 30%
faster and the evolution of the porosity perturbation is therefore completely different. This leads to the implication
that one should be careful in models where melt can move relatively to the matrix, as solitary porosity waves
always try to build up, even if the compaction length is not sufficiently resolved, and could lead to spurious
focusing and too high velocities that wouldn't be there with better resolution.

The introduced partition coefficients help distinguish between a solitary wave and diapirism but there is more
information needed, i.e. the matrix and fluid velocity, to really distinguish between the three regimes. For some
cases focusing into solitary waves can be observed despite diapirism being dominant. Not until the segregation
velocity becomes slower than the matrix, pure diapirism can be observed. These regimes might be not directly
applicable to different models e.g. with different amplitudes, rheology laws, permeability laws or background
porosities, but their well-defined existence shows that they should exist in generality and the models shown here
give an order of magnitude for which perturbation to compaction length ratios one needs to be careful.

The used equation for the Stokes velocity is valid for a sphere and not an infinite long cylinder like the initial
perturbation in our 2D model. But still, the velocities fit quite nicely to the observed model velocities. There is no
analytic solution for an infinite long cylinder in an infinite medium, but only the solution of a cylinder inside a
cylinder with finite radius, where the ratio of both cylinders has some influence on the velocity. For the size of the
initial cylindrical wave in a lager cylinder of characteristic size of our model box this solution is nearly identical
to the solution of a sphere and therefore it doesn't make sense to use the mathematically more complex solution
of a cylinder.

5 Conclusion

This work shows that, depending on the extent of a partially molten region within the earth, the resulting ascent of
melt may not only occur by solitary waves or by diapirs, but by an intermediate new mechanism which we call
"solitary wave induced focusing". Depending on the ratio of the melt anomalies size to the compaction length,
quantitatively we can classify the ascent behavior into three different regimes using mass flux and velocity of
matrix and melt: (1) Solitary wave a and b, (2) Solitary wave induced focusing and (3) diapirism. In regime 1a the
matrix sinks with respect to the rising melt, in 1b also the matrix rises, but very slowly. On first order these regimes
can be explained by comparing Stokes velocity of the rising perturbation with the solitary waves phase velocity.
If the Stokes velocity is higher a diapir will evolve, if lower, a solitary wave will evolve. But even if the Stokes

velocity is higher, solitary waves are attractors and might be able to focus melt locally within the rising diapiric plume. These focused fingers have a scale of the order of one compaction length, i.e. they have a scale at which

290 melt channeling instabilities are expected to occur. Not until the segregation velocity becomes smaller than the matrix velocity, solitary waves are no longer able to evolve.

Especially in the second regime numerical resolution plays an important role as the compaction length might be no longer resolved properly. This lack of proper resolution could lead to too big solitary waves, limited by the grid size, and therefore to too high velocities and magma fluxes. Hence it should be generally important for two-phase

295 flow models to inspect the size of partially molten areas and anomalies with respect to resolution because this spurious focusing might lead to wrong conclusions. This work might help to identify such scenarios, depending on partial melt anomaly to compaction length ratio, where problems might occur.

Code availability

The used finite difference code, FDCON, is available on request.

300 **Author Contribution**

Janik Dohmen wrote this article and carried out all models shown here. Harro Schmeling helped preparing this article and had the idea for this project.

References

Barcilon, V., & Lovera, O. M.: Solitary waves in magma dynamics. *Journal of Fluid Mechanics*, *204*(1989),

305 121–133. https://doi.org/10.1017/S0022112089001680, 1989.

Bittner, D., & Schmeling, H.: Numerical modelling of melting processes and induced diapirism in the lower crust. *Geophysical Journal International*, *123*(1), 59-70, 1995.

Connolly, J. A. D.: Devolatilization-generated fluid pressure and deformation-propagated fluid flow during prograde regional metamorphism. *Journal of Geophysical Research: Solid Earth*, *102*(B8), 18149-18173,

310 1997.

Connolly, J. A. D., & Podladchikov, Y. Y.: Compaction-driven fluid flow in viscoelastic rock. *Geodinamica Acta*, *11*(2–3), 55–84. https://doi.org/10.1080/09853111.1998.11105311, 1998.

Connolly, J. A. D., & Podladchikov, Y. Y.: A hydromechanical model for lower crustal fluid flow. In *Metasomatism and the chemical transformation of rock* (pp. 599-658). Springer, Berlin, Heidelberg,

315 2013.

Dohmen, J., Schmeling, H., & Kruse, J. P.: The effect of effective rock viscosity on 2-D magmatic porosity waves. *Solid Earth*, *10*(6), 2103-2113, 2019.

Griffiths, R. W.: The differing effects of compositional and thermal buoyancies on the evolution of mantle diapirs. *Physics of the earth and planetary interiors*, *43*(4), 261-273, 1986.

320   Jordan, J. S., Hesse, M. A., & Rudge, J. F.: On mass transport in porosity waves. *Earth and Planetary Science Letters*, *485*, 65–78. https://doi.org/10.1016/j.epsl.2017.12.024, 2018.

McKenzie, D.: The generation and compaction of partially molten rock. *Journal of Petrology*, *25*(3), 713–765. https://doi.org/10.1093/petrology/25.3.713, 1984.

Omlin, S., Malvoisin, B., & Podladchikov, Y. Y.: Pore Fluid Extraction by Reactive Solitary Waves in 3-D.
325   *Geophysical Research Letters*, *44*(18), 9267–9275. https://doi.org/10.1002/2017GL074293, 2017.

Richard, G. C., Kanjilal, S., & Schmeling, H. (2012). Solitary-waves in geophysical two-phase viscous media: A semi-analytical solution. *Physics of the Earth and Planetary Interiors*, *198–199*, 61–66. https://doi.org/10.1016/j.pepi.2012.03.001

Rubin, A. M.: Propagation of magma-filled cracks. *Annual Review of Earth and Planetary Sciences*, 287–336,
330   1995.

Schmeling, H.: Partial melting and melt segregation in a convecting mantle. In *Physics and Chemistry of Partially Molten Rocks*. Springer, 2000.

Schmeling, H., Marquart, G., Weinberg, R., & Wallner, H.: Modelling melting and melt segregation by two-phase flow: New insights into the dynamics of magmatic systems in the continental crust. *Geophysical
335   Journal International*, *217*(1), 422–450. https://doi.org/10.1093/gji/ggz029, 2019.

Scott, D. R., & Stevenson, D. J.: Magma solitons. *Geophysical Research Letters*, *11*(11), 1161–1164, 1984.

Simpson, G., & Spiegelman, M.: Solitary wave benchmarks in magma dynamics. *Journal of Scientific Computing*, *49*(3), 268–290. https://doi.org/10.1007/s10915-011-9461-y, 2011.

Spiegelman, M.: Physics of Melt Extraction: Theory, Implications and Applications. *Philosophical Transactions
340   of the Royal Society A: Mathematical, Physical and Engineering Sciences*, *342*(1663), 23–41. https://doi.org/10.1098/rsta.1993.0002, 1993.

Spiegelman, M.: Flow in deformable porous media. Part 2 Numerical analysis - the relationship between shock waves and solitary waves. *J. Fluid Mech.*, *247*, 39–63. https://doi.org/10.1017/S0022112093000370, 1993.

Šrámek, O., Ricard, Y., & Bercovici, D.: Simultaneous melting and compaction in deformable two-phase media.
345   *Geophysical Journal International*, *168*(3), 964–982. https://doi.org/10.1111/j.1365-246X.2006.03269.x, 2007.

Stevenson, D. J.: Spontaneous small-scale melt segregation in partial melts undergoing deformation. *Geophysical Research Letters*, *16*(9), 1067-1070, 1989.

Watson, S., & Spiegelman, M.: Geochemical Effects of Magmatic Solitary Waves—I. Numerical Results.
350   *Geophysical Journal International*, *117*(2), 284–295. https://doi.org/10.1111/j.1365-246X.1994.tb03932.x, 1994.

Solid Earth

Discussions

Open Access

EGU

Wiggins, C., & Spiegelman, M.: Magma migration and magmatic solitary waves in 3D. *Geophysical Research Letters*, *22*(10), 1289–1292. https://doi.org/10.1029/95GL00269, 1995.

Yarushina, V. M., Podladchikov, Y. Y., & Connolly, J. A. D.: (De)compaction waves in porous
355   viscoelastoplastic media: Solitary porosity waves. *Journal of Geophysical Research: Solid Earth*, 1–20.
https://doi.org/10.1002/2014JB011260.Received, 2015.
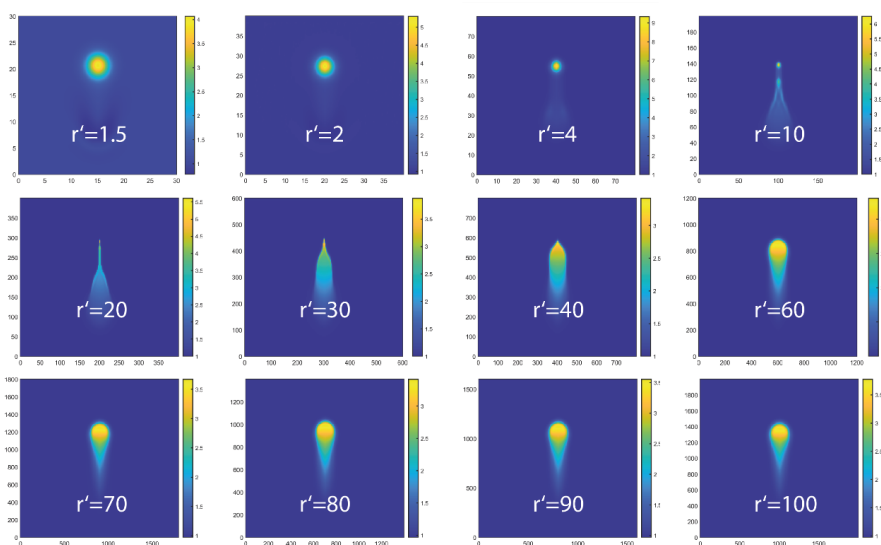
Fig. 1: Resulting melt fraction fields after the maximum melt fraction in the model has reached 70% of the boxes height for different initial perturbation sizes. All shown quantities are non-dimensional. The initial
360   **perturbation radius of the model is given in white in terms of compaction lengths. All quantities shown are non-dimensional.**
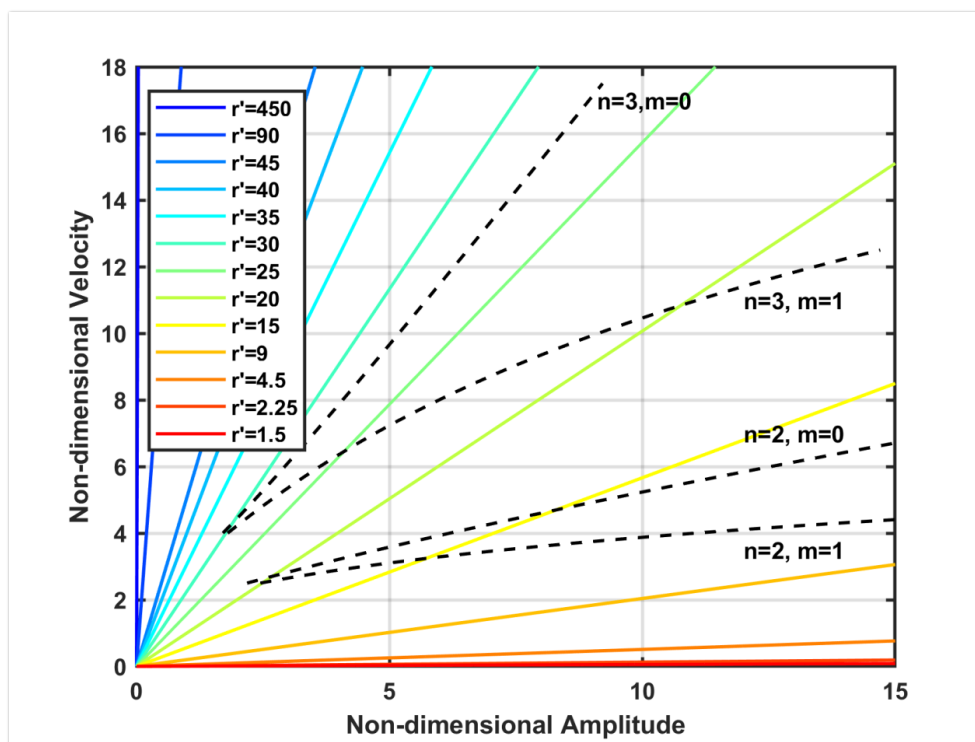
Fig. 2: The dashed lines give the dispersion relation for solitary waves, with different n's and m's, calculated semi-analytically by Simpson & Spiegelman (2012). The colored lines show the velocity of a Stokes sphere

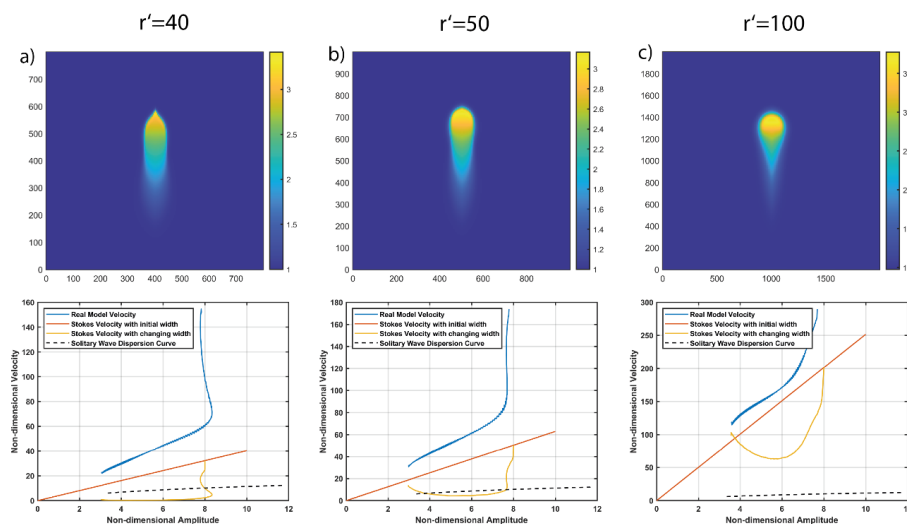365   **with a certain non-dimensional radius as a function of non-dimensional porosity amplitudes.**
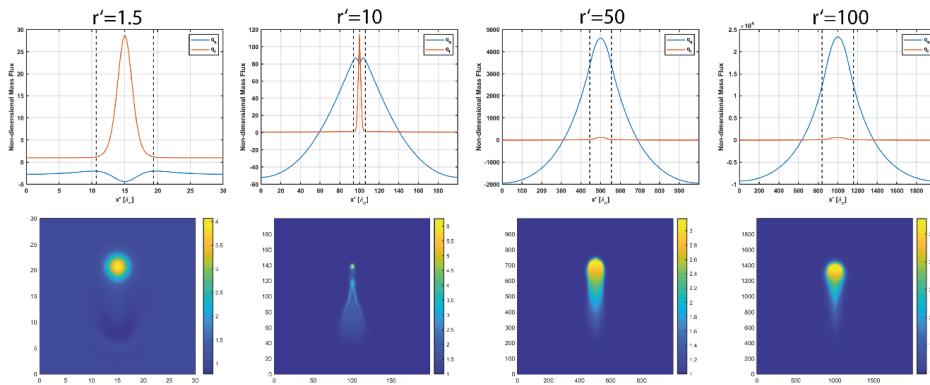

Fig. 3: The upper row gives melt fractions for three different initial perturbation radii after the maximum

melt fraction has reached 70% of the models height: (a) r'=40, (b) r'=50, (c) r'=100. The lower row gives

velocities as a function of porosity amplitude. The dashed lines give the ideal solitary wave dispersion
370   relation for our model and code, the red lines give the Stokes velocity for a sphere with constant radius, the
yellow lines give the Stokes velocity for a radius updated at every time step and blue lines show the rising
velocity of the maximum melt fraction in the model. All quantities shown are non-dimensional.

Fig. 4: The upper row gives the solid and fluid mass fluxes of a horizontal line cutting through the maximum
375   melt fraction of the model after it has reached 70% of the models height for different initial perturbation
radii. The bottom row gives the corresponding melt porosity fields. All quantities shown are non-
dimensional.
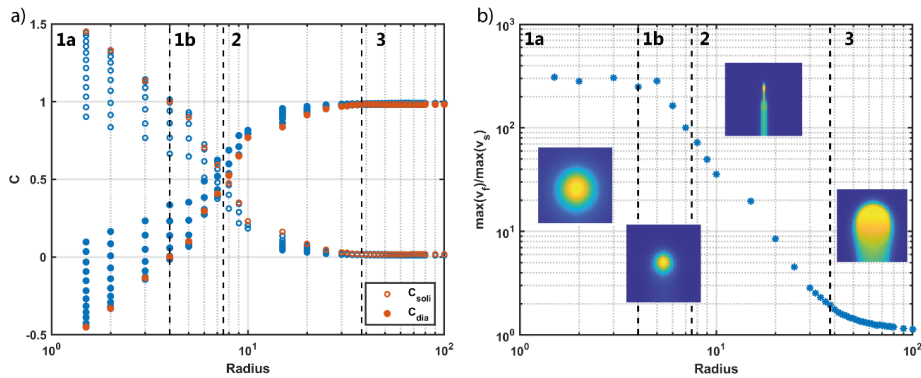
Fig. 5: a) The graph shows the solitary wave and diapir partition coefficients for several initial perturbation
380   radii. The red dots give the coefficients calculated on a horizontal line at the height of maximum melt
fraction. All blue dots give the coefficients calculated at all grid points below the maximum melt fraction as
long as at these horizontal lines maximum melt fraction is higher than half the models maximum. The
dashed lines are the borders of the regimes. Figure b) shows the ratio of maximum fluid velocity to
maximum solid velocity in the whole model. The small pictures show typical melt fraction perturbations for
385   each regime. The pictures are from models with an initial perturbation radius of 2, 6, 20 and 60 from left to
right.